ARCHIVES OF ELECTRICAL ENGINEERING VOL. 68(3), pp. 677–695 (2019)

DOI 10.24425/aee.2019.129350

Scaling laws for the FE solutions of induction machines

MARTIN NELL[1], JONAS LENZ[2], KAY HAMEYER[1]

[1] *RWTH Aachen University, Institute of Electrical Machines (IEM)*
Schinkelstraße 4, 52062 Aachen, Germany
e-mails: martin.nell@iem.rwth-aachen.de

[2] *Ulm University, Institute of Energy Conversion and Storage*
Albert-Einstein-Allee 47, 89081 Ulm, Germany

(Received: 22.05.2019, revised: 23.05.2019)

Abstract: In this paper a scaling approach for the solution of 2D FE models of electric machines is proposed. This allows a geometrical and stator and rotor resistance scaling as well as a rewinding of a squirrel cage induction machine enabling an efficient numerical optimization. The 2D FEM solutions of a reference machine are calculated by a model based hybrid numeric induction machine simulation approach. In contrast to already known scaling procedures for synchronous machines the FEM solutions of the induction machine are scaled in the stator-current-rotor-frequency-plane and then transformed to the torque-speed-map. This gives the possibility to use a new time scaling factor that is necessary to keep a constant field distribution. The scaling procedure is validated by the finite element method and used in a numerical optimization process for the sizing of an electric vehicle traction drive considering the gear ratio. The results show that the scaling procedure is very accurate, computational very efficient and suitable for the use in machine design optimization.

Key words: evolutionary strategy, finite element method analysis, induction machine, induction motor, loss calculation, multi-objective optimization, scaling laws

1. Introduction

Energy optimization performed for example by an improvement in the efficiency of electrical equipment is the global trend today [1]. In developed countries the industrial induction machines (IMs) are the major consumers of electric energy and globally account for about 40% of overall power consumption [2].

To lead manufacturers to design and build more efficient IMs the European Union specified the new premium efficiency standard (IE3) for IMs operated at 50 Hz or 60 Hz by the IEC

60034-30 standard [3]. Since January 1, 2015 this standard is valid for IMs with a rated power of 7.5 to 375 kW and since January 1, 2017 for IMs with a rated power of 0.75 to 375 kW. The standard also reserves an IE4 class for the future.

Due to the low-cost, ruggedness and fault tolerance, frequency-inverter-driven IMs are used as the main workhorse in the rising market of electrical and hybrid drive trains [4]. Here too, however, the main aim is to reduce the energy consumption or, in other words, to improve the efficiency of the drive train and particularly of the IM [15]. Moreover, in electric or hybrid vehicles minimum cost and weight are further goals [15]. Proficient manufacturers have the experience to design high premium efficient electrical machines. But only mathematical optimization can handle the complexity of the relations between the machine's geometry and its performance and nonlinearity [5] in a short time. With the mathematical optimization tool the limits can be pushed toward more efficient designs. For the design of high efficient IMs, particularly for frequency-inverter-driven ones, a detailed loss analysis is required. This requires local and temporal highly resolved nonlinear field computation and can be performed in the post processing of nonlinear transient finite element simulations of the magnetic circuit [16].

For the IM, the finite element method (FEM) takes a large number of simulation time steps to build up the machine's rotor flux matrix [16]. Hence, using the time-consuming FEM in a mathematical optimization procedure would end up in an extremely time-consuming calculation and therefore is not suitable. Von Pfingsten, Nell and Hameyer [6, 16] proposed a hybrid simulation approach for the IMs 2D finite element (FE) calculation that drastically decreases the simulation time by shortening the transient build-up of the rotor flux. Nevertheless, this hybrid approach, that needs about 2 000 core hours for an efficiency map, is still not sufficient for the application in a mathematical optimization procedure.

Due to the fact that the FEM and other numerical methods are very time-consuming scaling laws are a popular method in physics and engineering. They are often used in numerous examples. Wood [7] described the general scaling laws for electromagnetic systems. His work was motivated by the constraint of the system's thermal stability. By using the electromagnetic and thermal diffusion equation, as well as the momentum and kinematic equation Hsieh and Kim [8] presented a detailed derivation of scaling laws for electromechanical systems.

2. Scaling laws of electrical machines

Žarko, Stipetič and Ramakrishnan published several papers about the scaling laws for synchronous machines (SM). In [17] and [9] the procedures of radial and axial geometrical scaling and of rewinding for the SM are introduced. In [18] the efficiency maps of the SM are calculated by using a scalable saturated flux linkage and loss model of the SM. In [15] and [19] the scalable SM models are used to find the optimal sizing of a SM traction motor. Moreover, Žarko presented a method to design a premium efficiency IM, using scaling laws for its equivalent circuit parameters in [2]. He assumed that the temperature rise in the slot of the original and the scaled motor are similar.

Another method to improve the IM efficiency classes, using the method to scale the core axial lengthening, was described by Alberti, Bianchi, Boglietti and Cavagnino in [10]. The influence of the rotor diameter and the length on the rating of IMs was presented by Bone in [11]. His scaling

laws for IMs are not as exact as the ones derived in this paper because the field solutions change. Nonetheless, they are well applicable for machine designers. In this paper a more sophisticated approach for a mathematical optimization of squirrel cage IMs is discussed. It is based, on the one hand, on the hybrid simulation approaches for induction machine calculation from von Pfingsten, Nell and Hameyer [6, 16], and on the other hand, on the scaling laws for the IMs proposed in this paper and in [20]. The procedure of this method is illustrated in Fig. 1. The stator-current-slip-frequency-operation-planes (I_1–f_2-planes) of a reference machine design are calculated with the hybrid simulation approach of von Pfingsten, Nell and Hameyer [6, 16].

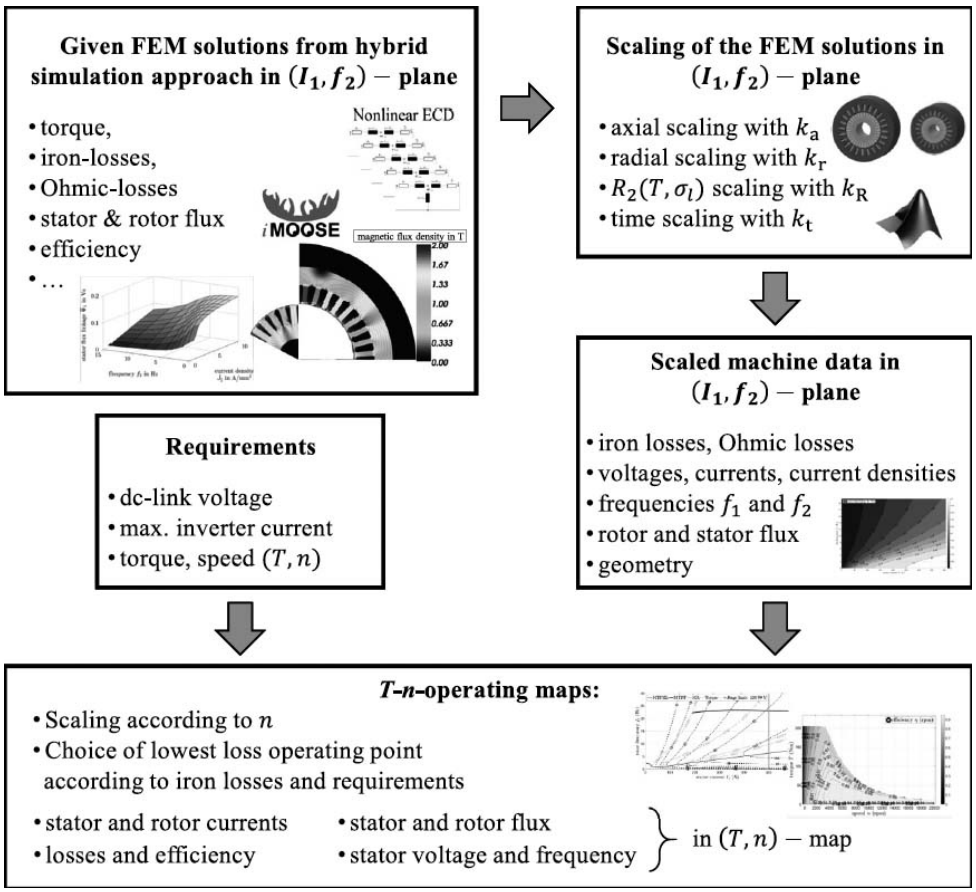

Fig. 1. Machine scaling scheme

To obtain a new scaled motor design the solutions are scaled in the I_1–f_2-plane without changing the field solution of the IM. Taken into account requirements, such as dc-link voltage, maximum inverter current, and the operation strategy, such as Maximum Torque Per Ampere (MTPA) or Maximum Torque Per Electrical Losses (MTPELs), the I_1–f_2-planes are transformed to torque-speed-maps (T-n-maps).

3. Modeling of an induction machine

3.1. IM operating points in terms of the I_1-f_2-plane

The fundamental wave T-equivalent-circuit of an IM is presented in Fig. 2. It demonstrates the allocation of the stator current I_1 into the magnetizing current I_μ and the rotor current related to the stator side I_2^S. Moreover, it illustrates that all reactances and the rotor resistance R_2^S are proportional to the synchronous angular frequency ω_1. According to von Pfingsten, Nell and Hameyer in [6, 21] and [16] the allocation of the stator current I_1 into the magnetizing current I_μ and the rotor current I_2^S is independent of the stator frequency f_1 by subtracting the voltage drop on the stator resistance R_1. As a result, this allocation only depends on the rotor frequency f_2 and the saturation of the main inductance L_M. The saturation has to be considered in highly utilized traction drives and occurs at high values of I_μ that is reached at low values for f_2 and high values for I_1 [21]. Therefore, the current allocation of I_1 into I_μ and I_2^S only depends on the amplitude of the stator current I_1 and the rotor current frequency f_2, as long as the rotor resistance and the inductances are assumed to be constant. All torque speed operating points of an IM with a constant rotor resistance R_2^S can be mapped in the I_1-f_2-plane.

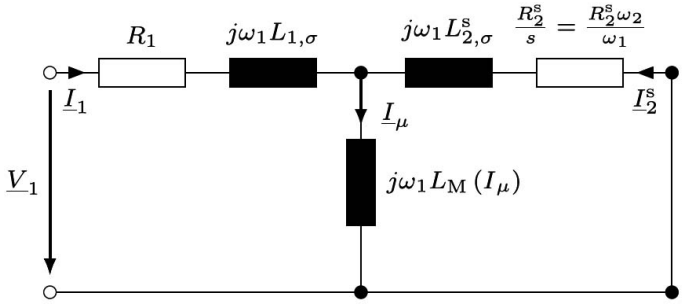

Fig. 2. Equivalent circuit diagram of a squirrel cage induction machine

3.2. Induction machine calculation applying the hybrid simulation approach

To accelerate the FE calculation of the IM, the hybrid simulation approach presented in [6] and [16] is used. With the hybrid simulation approach, the entire I_1-f_2-plane and T-n-map, respectively, can be calculated 50% faster than with the transient FEM. In combination with the hereafter introduced scaling scheme it provides a fast procedure to calculate and scale IMs that leads to the possibility of the use for numerical optimization. The main aspects of it will be described in the following.

In the first step, a non-linear no-load static finite element analysis (FEA) with one simulation time step is conducted $k = 1, \ldots, K$ times, where k marks a certain saturation state [6, 16]. The stator current I_1 is the only excitation. For each non-linear no-load FEA the inductance matrix $\boldsymbol{L}(k)$ of the IM is extracted in accordance with [12]. From these extracted matrices $\boldsymbol{L}(k)$ the rotor current I_2^S is calculated with the analytical fundamental wave equations derived from the equivalent circuit diagram in Fig. 2 for every saturation state k. With the stator current vector $\vec{\underline{I}}_1$ and the saturation dependent rotor current vector $\vec{\underline{I}}_2^S$, the stator flux linkage vector $\vec{\underline{\Psi}}_1(k)$ for every

saturation state k is calculated. By comparing the amplitude of this stator flux linkage and the no-load stator flux linkage of the no-load FEA $\underline{\vec{\Psi}}_{1,nl}(k)$ the valid saturation state is found. With numerical interpolation, the value of the rotor current for each operating point in the I_1-f_2-plane is found and used as the excitation for the second, now transient, FE simulation [6, 16]. The calculation steps are performed in the I_1-f_2-plane with the fixed stator frequency f_1 and fixed rotor resistance R_2^S, as well as the rotor conductivity σ_2, respectively.

By considering an operation strategy such as MTPEL and by scaling the loss power of the IM according to different synchronous speeds f_1, as described in [4], the I_1-f_2-plane is transformed to the T-n-map. A variation of the rotor resistance R_2^S by temperature can be considered with the scaling laws of the rotor resistance due to the temperature variations described in section 4.6.

4. Scaling laws for induction machines

The previous scaling laws for IMs introduced by Bone in [11] are not exact due to the fact that the field solution is changed. The IM scaling laws of Žarko in [2] deal with scaling the IM's equivalent circuit parameters assuming equal temperature rise in the slots of the original and reference motor. For the SM, Stipetič, Žarko and Popescu derived scaling laws that consider the same field solution. This is the basis for the IM scaling laws in this paper. In the following the scaled parameters are marked with ($'$).

4.1. Geometrical scaling

The geometrical scaling in cylindrical systems is subdivided into radial and axial scaling with the radial scaling factor k_r and the axial scaling factor k_a. The effect of the geometrical scaling is pictured in Fig. 3 and described with

$$\rho' = \rho k_r\,, \tag{1}$$

$$l' = l k_a\,, \tag{2}$$

$$A'_{\text{cross}} = A_{\text{cross}} k_r^2\,, \tag{3}$$

$$A'_{\text{surface}} = A_{\text{surface}} k_r k_a\,, \tag{4}$$

$$V' = V k_r^2 k_a\,, \tag{5}$$

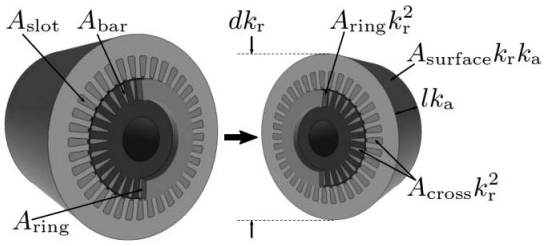

Fig. 3. Scaled machine parameters

where l is the axial length, ρ is the radial distance to the center, A_{cross} is the cross-section areas, A_{surface} is the radial surface area and V is the volume of the active part of the machine. The cross-section of the short-circuit ring also increases with k_r^2 and is independent of k_a to preserve a constant relation to the bar cross-section. The conductor cross-section also changes with k_r^2. For the end windings it is assumed that the conductor length increases quadratically with k_r since the conductor cross-sections increase, thus the axial extent becomes larger and the arc length increases linearly with k_r.

4.2. Centrifugal force

The rotation or the angular velocity ω respectively of the rotor of an IM causes a centripetal force, orthogonal to the motion and towards the center of the rotor. The centripetal force

$$F_\rho = m\rho\,\omega^2 \tag{6}$$

is proportional to the mass of the rotor m and the radial distance to the center ρ. The fictitious centrifugal force that is directed away of the rotation axis, is a reaction to the centripetal force. The centripetal force causes a tension

$$\sigma = \frac{m\rho\,\omega^2}{A}, \tag{7}$$

where A is the area at which the force acts. To avoid plastic deformations in the materials of the rotor at high rotational speeds the tension in the materials must not exceed the maximum tension $\sigma_{\max}$. Therefore, the angular velocity has to be limited to

$$\omega_{\max} = \sqrt{\frac{\sigma_{\max} A}{m\rho}}. \tag{8}$$

With the geometric scaling relations in (4) and (1) and the mass, scaled with $k_a k_r^2$, the scaling law for the maximum rotor speed

$$n'_{\max} = n_{\max}\frac{1}{k_r} \tag{9}$$

is derived.

4.3. Scaling of the electrical and magnetic parameters

Due to the fact that the magnetic permeability μ is in a non-linear relation to the magnetic field strength $\vec{\boldsymbol{H}}$, one assumption of scaling the FE solutions is that the magnetic field strength distribution inside the IM does not change. Therefore,

$$\vec{\boldsymbol{H}}'(\rho', \varphi') = \vec{\boldsymbol{H}}(\rho, \varphi) \tag{10}$$

is applicable.

In accordance with Ampère's law

$$\vec{\boldsymbol{J}}' = \nabla' \times \vec{\boldsymbol{H}}' = \frac{1}{\rho}\left[\frac{\partial}{\partial \rho'}(\rho' H'_\varphi) - \frac{\partial H'_\rho}{\partial \varphi'}\right]\vec{e}_z, \tag{11}$$

with the polar coordinates ρ and φ, as well as the unit vector $\vec{e}_z$ the scaling dependence of the electric current density

$$\vec{\boldsymbol{J}}' = \frac{1}{k_r}\nabla \times \vec{\boldsymbol{H}} = \frac{1}{k_r}\vec{\boldsymbol{J}} \tag{12}$$

follows.

In [8] it is described that a scaling factor k_{t1} has to be used to satisfy that the magnetic flux density B is kept constant $B(\rho, \varphi) = B'(\rho', \varphi')$ and therefore the equality of the magnetic field strength (10) is satisfied. With the assumption that the geometrical dimensions are clearly shorter than the magnetic wave length Ampère's circuital law with Maxwell's addition is simplified to Ampère's law:

$$\nabla \times \vec{\boldsymbol{H}} = \sigma \vec{\boldsymbol{E}}. \tag{13}$$

With Faraday's law of induction

$$\nabla \times \vec{\boldsymbol{E}} = \frac{\partial \vec{\boldsymbol{B}}}{\partial t} \tag{14}$$

and mathematical transformations

$$k_{t1}\frac{\partial \vec{\boldsymbol{B}}'}{\partial t'} + k_r^2 \nabla' \times \frac{1}{\sigma}\left(\nabla' \times \frac{\vec{\boldsymbol{B}}}{\mu}\right) = 0 \tag{15}$$

is derived, where σ is the electric conductivity and $\vec{\boldsymbol{E}}$ is the electric field strength. The assumption that the magnetic field strength, and therefore, the magnetic flux density do not change during scaling, leads to

$$k_{t1} = k_r^2\,. \tag{16}$$

Hence, the time scaling factor k_{t1} corresponds to the square of the radial scaling factor k_r. As a result, all time depending parameters have to be scaled by the total time scaling factor k_t, which is the product of the first time scaling factor k_{t1} and the second one k_{t2}. The second time scaling factor is a result of the rotor resistance scaling and will be discussed in detail in section 4.5 and 4.6. The time scaling leads to the proportionality of the reactances to the reciprocal time scaling factor shown in Fig. 4.

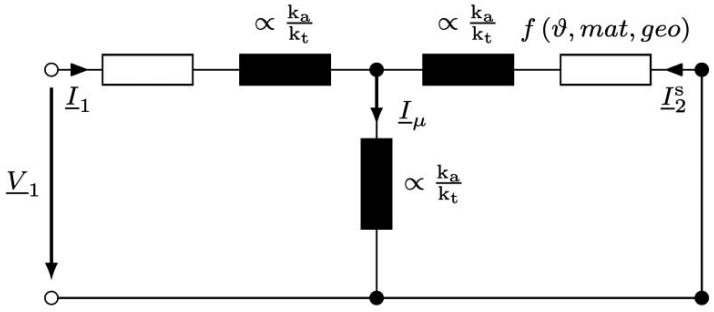

Fig. 4. Scaling factor dependencies of the elements of the equivalent circuit diagram of a squirrel cage induction machine

The magnetic flux Ψ, which is proportional to the inductance, scaled with k_a and the current, scaled with k_r, changes with $k_a k_r$:

$$\Psi' = k_r k_a \Psi. \tag{17}$$

From (3) and (12) it follows that the current changes with k_r:

$$I' = k_r I. \tag{18}$$

The machine's torque T_{elec} is dependent on the flux and current. Hence, the torque is scaled in accordance to:

$$T'_{\text{elec}} = \frac{3}{2} p \left(I_{q,1} k_r \Psi_{d,1} k_r k_a - I_{d,1} k_r \Psi_{q,1} k_r k_a \right) = T_{\text{elec}} k_r^2 k_a \,. \tag{19}$$

4.4. Stator resistance scaling

The stator resistance of an IM has to be scaled separately according to the winding head and the axial length of the stator iron l_{Fe}, that is independent of the radial scaling k_r and proportional to k_a. It is assumed that the conductor length in the winding head l_{WH} increases linearly with k_r, since firstly, the conductor cross-sections increase and thus the axial expansions of the winding head become larger and secondly, the arc length increases linearly with k_r. The conductor cross-sections A_{wire} themselves increase with k_r^2. This leads to the scaled stator resistance:

$$R'_1 = 2 N_1 \frac{l_{\text{Fe}} k_a + l_{WH} k_r}{\sigma_1 A_{\text{wire}} k_r}, \tag{20}$$

where σ_1 is the conductivity of the winding material and N_1 is the number of stator slots.

4.5. Rotor resistance scaling due to geometric variations

The equivalent circuit of the IM in Fig. 2 shows that the rotor resistance related to the stator side R_2^S and therefore the rotor resistance R_2 has a major impact on the machine's behavior. In contrast to the scaling of the SM done by Žarko, Stipetič and Ramakrishnan in IMs the scaling of the rotor resistance is an important step. In addition to the varied rotor resistance due to the geometrical scaling the resistance can vary because of temperature, material and electric conductivity variations, respectively. The consequence of the geometrical scaling has to be considered separately in terms of the bar resistance R_{bar} and the resistance of the short-circuit ring R^*_{ring}. The resistance of the rotor bar can be described with

$$R_{\text{bar}} = \frac{l_{\text{Fe}}}{\sigma_2 A_{\text{bar}}} \propto \frac{k_a}{k_r^2}, \tag{21}$$

where l_{Fe} is the active length of the IM, A_{bar} is the area of the rotor bar and σ_2 is the conductivity of the rotor conductors, and it is proportional to $\dfrac{k_a}{k_r^2}$. The resistance of a short circuit ring segment ΔR_{ring} can be described by:

$$\Delta R_{\text{ring}} = \frac{2\pi r_{\text{ring}}}{\sigma_2 A_{\text{ring}} Q_2} \propto \frac{k_r}{k_r^2} = \frac{1}{k_r}, \tag{22}$$

where r_{ring} describes the middle radius of the short-circuit ring, A_{ring} is the area of the short-circuit ring and Q_2 is the rotor bar number. According to [13] this resistance can be transformed to an equivalent series resistance ΔR^*_{ring} described by

$$\Delta R^*_{\text{ring}} = \Delta R_{\text{ring}} \cdot \frac{1}{\left(2\sin\left(\frac{\pi p}{Q_2}\right)\right)^2} \propto \frac{1}{k_r}, \tag{23}$$

with the number of pole pairs p, which is used in the 2D FEM. As outlined in section 4.1 the cross-section area of the short-circuit ring increases with k_r^2 and is independent of the axial scaling. Therefore, ΔR^*_{ring} is proportional to the inverse of the radial scaling factor k_r as in (23). The addition of the bar resistance and the equivalent series resistance of the short-circuit ring lead to the total resistance of the rotor

$$R_2 = R_{\text{bar}} + 2\Delta R^*_{\text{ring}}. \tag{24}$$

By defining a compensating conductivity

$$\sigma_{2,\text{comp}} = \frac{l_{\text{Fe}}}{A_{\text{bar}} R_2} \propto \frac{k_a}{k_r^2 \cdot k(R_2)}, \tag{25}$$

it leads to a rotor resistance scaling factor

$$k_{R1} = \frac{\sigma_{2,\text{comp}}}{\sigma'_{2,\text{comp}}} = \frac{\dfrac{1}{R_{\text{bar}} + 2\Delta R^*_{\text{ring}}}}{\dfrac{k_a}{k_r^2\left(R_{\text{bar}}\dfrac{k_a}{k_r^2} + 2\Delta R^*_{\text{ring}}\dfrac{1}{k_r}\right)}}, \tag{26}$$

which can be simplified to

$$k_{R1} = \frac{\sigma_{2,\text{comp}}}{\sigma'_{2,\text{comp}}} = 1 + \left(\frac{k_r}{k_a} - 1\right)\kappa_2, \tag{27}$$

with

$$\kappa_2 = \frac{1}{\dfrac{l_{\text{Fe}}}{\pi_{\text{ring}}}\dfrac{A_{\text{ring}}}{A_{\text{bar}}} Q_2 \sin^2\left(\dfrac{\pi p}{Q_2}\right) + 1}$$

as the rotor geometry constant that is defined for the unscaled machine. The scaling factor k_{R1} describes the variation of the rotor resistance due to a variation in the relation of the axial length and radial length, expressed by $\dfrac{k_r}{k_a}$ of the machine. If the relation is kept constant k_{R1} is equal to one.

4.6. Rotor resistance scaling due to rotor conductivity variations

The scaling of the rotor resistance in accordance to the scaling of the compensating rotor conductivity leads to further possibilities of rotor resistance scaling. The rotor conductivity and

resistance, respectively, can vary due to a variation of the material or by temperature. Hence, a second rotor resistance scaling factor

$$k_{R2} = \frac{\sigma_2}{\sigma_{2,\text{new}}} \frac{1 + \alpha_{\text{new}}(\vartheta_{\text{sim,new}} - \vartheta_{\text{ref,new}})}{1 + \alpha(\vartheta_{\text{sim}} - \vartheta_{\text{ref}})} \tag{28}$$

is introduced. It is dependent on the old and new conductivity, σ_2 and $\sigma_{2,\text{new}}$, the old and new temperature coefficients α and α_{new}, the old and new reference temperatures ϑ_{new} and $\vartheta_{\text{ref,new}}$ and the old and new simulation temperatures ϑ_{sim} and $\vartheta_{\text{sim,new}}$. The resulting scaling factor for the rotor resistance can be calculated by the total scaling factor of the rotor resistance k_R and leads to the scaled rotor resistance:

$$R_2' = R_2 k_R\,, \quad \text{with } k_R = k_{R1} \cdot k_{R2} \cdot \frac{k_a}{k_r^2}\,. \tag{29}$$

In (29) the first part of the total rotor scaling factor k_{R1} considers a variation in the relation of the axial to the radial length of the machine. The second part k_{R2} considers a variation in the temperature or the conductivity of the rotor bars and rings. The last part $\frac{k_a}{k_r^2}$ considers the geometric variation of the rotor bars due to an axial and radial scaling of the IM. Fig. 4 shows that the rotor resistance is dependent on the temperature, material and geometry of the IM. To satisfy (10) the allocation of I_2^S and I_μ must not vary. As long as the rotor resistance is kept constant and the calculation of the machine is done in the I_1-f_2-plane, as described in section 3.1, (10) is valid. With a variation in R_2 the allocation changes. To ensure the same current allocation, even in the event of a variation in the rotor resistance, the condition that the ratio of the axial to the time scaling factor must correspond to the total rotor resistance scaling factor

$$\frac{k_a}{k_t} \stackrel{!}{=} k_R \tag{30}$$

has to be fulfilled. As a result the time scaling is supplemented by a second time scaling factor

$$k_{t2} = \frac{k_a}{k_R k_{t1}} = \frac{1}{k_{R1} k_{R2}}\,. \tag{31}$$

Thus, the total time scaling factor results in

$$k_t = k_{t1} k_{t2}\,. \tag{32}$$

With these rotor scaling factors it is possible to scale the IM due to a variation of the rotor resistance. This variation can be a result of a variation in the conductivity of the rotor conductor by different materials, such as copper or aluminum, or by their different qualities, as well as by an alternating temperature. Differences in the machine's behavior due to a varying quality of the rotor bar material can be calculated very fast with the proposed scaling process. In addition, a variation of the rotor resistance due to the skin effect can be taken into account by using analytical formula to recalculate the rotor resistance. This scaling process can also be used in combination with a thermal model of the IM to simulate the machine in different operating points with varying temperature conditions.

4.7. Scaling the number of turns of the winding

In addition to a geometric scaling of the IM, a variation in the number of turns of the stator winding N_W can be useful. In an axially extended machine the induced voltage increases with k_a. As a result, the maximum voltage of the machine is reached for lower speed and thus the corner point is at lower speed. To compensate this, the induced voltage can be reduced by reducing the number of turns of the stator winding. This can be done in the post processing of the FE simulation but a scaling factor of the number of turns of the winding k_N enables shorter computation times as one complete execute of the post processing procedure. Since the number of turns is an integer number k_N, it is defined with:

$$N'_W = N_W k_N \,, \tag{33}$$

$$k_N = \frac{N'_W}{N_W} \,. \tag{34}$$

The proportionals for the scaling of the number of turns of the winding are collected in Table 1.

Table 1. Parameter proportionals for the scaling of the number of turns of the stator winding

Parameter	**Variable**	$\propto$
Number of turns of stator	N_W	k_N
Transformation ratio	a	k_N
Stator wire cross sectional area	A_{wire}	$\frac{1}{k_N}$
Stator current	I_1	$\frac{1}{k_N}$
Stator flux density	B	k_N
Stator resistance	R_1	k_N^2
Stator copper losses	$P_{L,\text{ohm},1}$	1
Stator voltage	V_1	$\frac{1}{k_N}$

4.8. Scaling of the IM losses

The losses of an IM can be distinguished in Ohmic losses $P_{L,\text{ohm}}$ and iron losses $P_{L,\text{Fe}}$. The Ohmic losses of the rotor $P_{L,\text{ohm},2}$ are proportional to $k_r^2 k_R$ as in:

$$P'_{L,\text{ohm},2} = P_{L,\text{ohm},2} k_r^2 k_R \,. \tag{35}$$

The scaled Ohmic losses of the stator $P'_{L,\text{ohm},1}$ have to be calculated with the scaled stator current I'_1 and the scaled stator resistance R'_1. This leads to the scaled Ohmic losses of the stator:

$$P'_{L,\text{ohm},1} = 3 \cdot I'^2_1 R'_1 \,, \tag{36}$$

$$P'_{L,\text{ohm},1} = 3 \cdot \left(I_1 \frac{k_r}{k_N} \right)^2 \cdot 2N_1 \frac{l_{\text{Fe}} k_a + l_{WH} k_r}{\sigma_1 A_{\text{wire}} k_r} k_N^2 \,. \tag{37}$$

The iron losses, in turn, can be separated into hysteresis, eddy current and excess losses [21]. All three parts have a different dependency on the frequency f. Hence, different scaling relations for the three iron loss components exist. The scaled iron loss power density $p'_{L,\mathrm{Fe}}$ is:

$$p'_{L,\mathrm{Fe}} = \left(k_{\mathrm{hyst}} B^{\alpha} \frac{f}{k_t} + k_{\mathrm{eddy}} B^2 \frac{f^2}{k_t^2} + k_{\mathrm{excess}} B^{1.5} \frac{f^{1.5}}{k_t^{1.5}} \right), \tag{38}$$

where k_{hyst}, k_{eddy} and k_{excess} are the hysteresis loss, eddy current loss and excess loss coefficient, respectively. With the iron loss power density and the iron mass m_{Fe}, scaled with $k_r^2 k_a$, the scaled iron loss power $P'_{L,\mathrm{Fe}}$ is:

$$P'_{L,\mathrm{Fe}} = p'_{L,\mathrm{Fe}} m_{\mathrm{Fe}} k_r^2 k_a \,. \tag{39}$$

All scaling laws for the IM are summarized in Table 2.

Table 2. Scaling factors for the machine's parameters

Parameter	**Variable**	$\propto$
Length	l	k_a
Lateral surface	A_{surface}	$k_a k_r$
Cross sectional area	A_{cross}	k_r^2
Volume	V	$k_a k_r^2$
Magnetic field strength	H	1
Magnetic field density	B	1
Magnetic field linkage	Ψ	$k_a k_r$
Current density	J	$\frac{1}{k_r}$
Current	I	k_r
Time	T	k_t
Frequency	f	$\frac{1}{k_t}$
Speed	n	$\frac{1}{k_t}$
Torque	T	$k_a k_r^2$
Voltage	V	$\frac{k_a k_r}{k_t}$
Inductance	L	k_a
Reactance	X	$\frac{k_a}{k_t}$
Rotor resistance	R_2	k_R
Mechanical power	P_{mech}	$\frac{k_a k_r^2}{k_t}$
Mechanical power density	p_{mech}	$\frac{1}{k_t} = \frac{k_R}{k_a}$

4.9. Validation of the scaling laws

To validate the scaling laws for IMs a reference motor is calculated with the FEM in the first path via the hybrid simulation approach described in section 3.2. In the second path, the geometry and the rotor resistance of the IM are scaled and an FE simulation is performed with the scaled machine. The FE solutions of the scaled IM are rescaled in the I_1-f_2-plane to the parameters of the reference machine regarding the procedure described in Fig. 1. Finally, the solutions in the I_1-f_2-plane are transformed to the T-n-map, considering the same requirements. The procedure is shown in Fig. 5. The scaling factors in this simulation are $k_r = 1.2$, $k_a = 1.1$ and $k_{R2} = 1/1.05$.

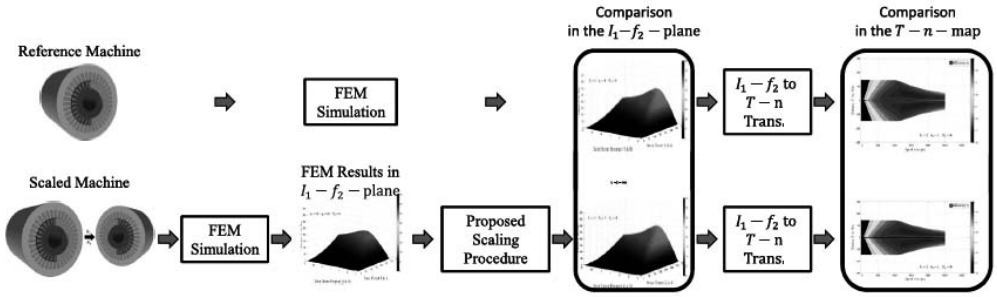

Fig. 5. Validation procedure of IM scaling

The results of the FE solutions of the reference machine (first path) and the rescaled FE solutions of the scaled machine (second path) are compared. The comparison is done in the I_1-f_2-plane and the T-n-map as described in Fig. 5. The calculated deviation of the loss power in the I_1-f_2-plane has a maximum error of $0.2 \cdot 10^{-3}$% that proves the correctness of the proposed scaling scheme. The comparison of the reference loss power and the loss power of the IM rescaled in the I_1-f_2-plane and transformed to the T-n-map is presented in Fig. 6. It also shows a very accurate performance of the proposed scaling procedure.

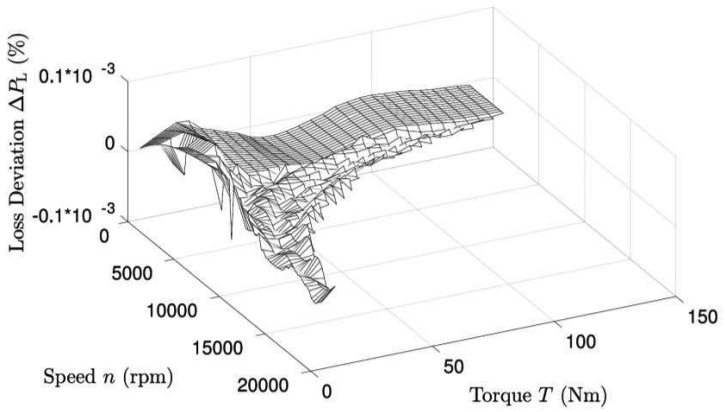

Fig. 6. Total loss deviation of the reference and the rescaled FE solutions in the T-n-map

In Fig. 7 the total losses transformed to the T-n-map of a reference IM machine and in Fig. 8 the total losses for a scaled machine, with the scaling factors $k_r = 1.2$, $k_a = 1.1$ and $k_{R_2} = 1/1.05$, are shown. For the transformation to the T-n-map the same requirements, such as the maximum frequency, the maximum inverter current and dc-link voltage and the operation strategy MTPEL, are taken into account. The maximum speed of the reference machine is set to 20 000 rpm which results in a maximum surface velocity of the rotor of 110 m/s. By increasing the radial dimension of the IM the speed limit has to be scaled according to (9). Thus, the maximum speed in Fig. 8 is about 16 666 rpm. In Fig. 9 the percentage deviation of the magnetic flux density ΔB in % of a reference IM and an IM whose geometrical dimensions are scaled with $k_r = 1.2$ and whose rotor bar conductivity is scaled with $k_{R2} = 1/1.2$ are shown. Here, the input parameter, such as the stator current I_1, the stator frequency f_1 or the rotor current frequency f_2 are not scaled resulting in a non-constant field distribution. Therefore, ΔB reaches values of more than 50%. Fig. 10 shows the percentage flux density deviation in the case that the input parameter are scaled due to the proposed scaling laws in Table 2. The maximum value of ΔB is 0.02%.

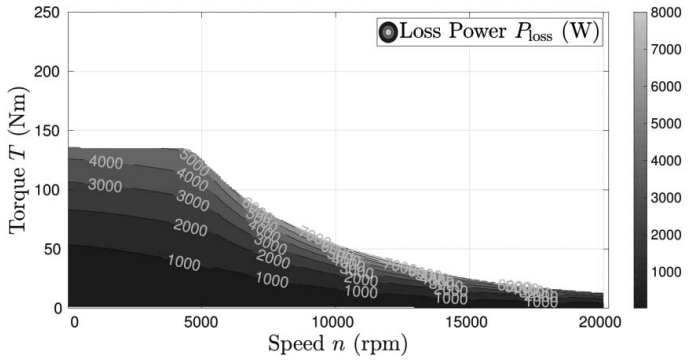

Fig. 7. Total losses of the reference IM machine

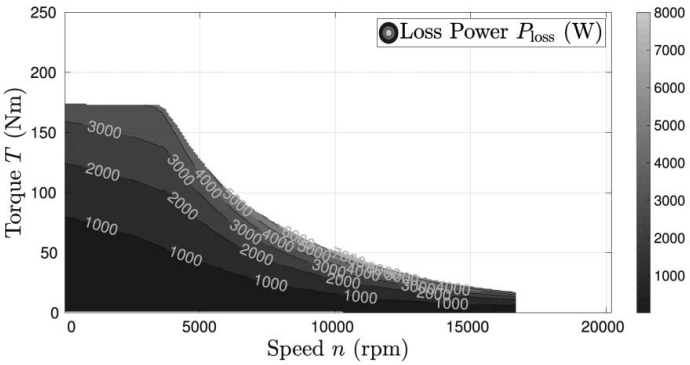

Fig. 8. Total losses of the scaled machine calculated with the scaling laws

It shows that with the proposed scaling laws the assumption of a constant flux distribution is fulfilled. For the calculation of ΔB the magnetic flux density B of the reference machine in each point (ρ, φ) is compared with the magnetic flux density of the scaled machine (B') in each point (ρ', φ') and mapped into the coordinates of the reference machine (ρ, φ).

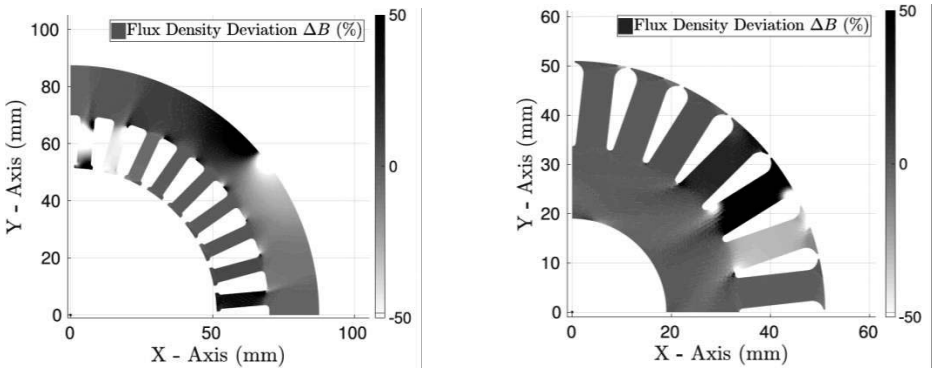

(a) (b)

Fig. 9. Deviation of the flux density ΔB in % for the stator (a) and rotor (b) of the reference and scaled IM without scaling of electrical parameters

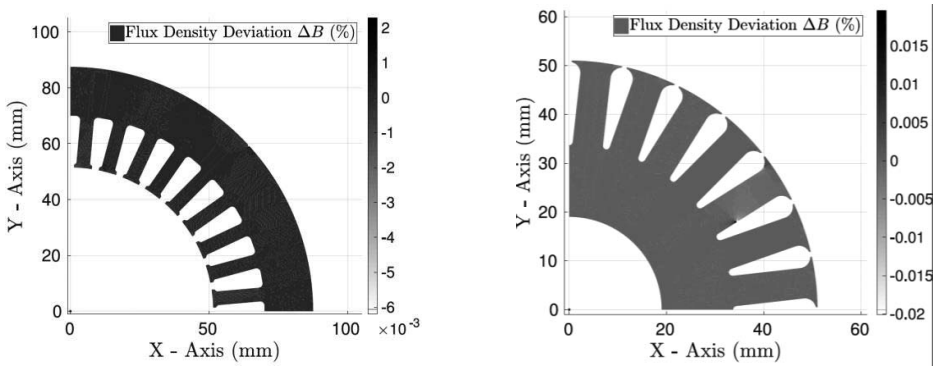

(a) (b)

Fig. 10. Deviation of the flux density ΔB in % for the stator (a) and rotor (b) of the reference and scaled IM with scaling of electrical parameters

5. Optimization of an induction machine for traction application

Due to its very fast performance, the proposed machine scaling scheme can be used in a numerical optimization procedure. In [22] Stipetič and Žarko present an overview of the methodology using mathematical optimization procedures to achieve an optimal design of an electrical machine. They suggest a metaheuristic algorithm, such as Evolution Strategy or Differential Evolution, for the complex electrical machine design. In [19], mixed integer distributed ant colony optimization is used to optimize a traction drive with a permanent magnet motor, calculated by using the FEM and geometrical scaling. In [14] multi-objective optimization in combination with the scaling laws of an SM is used to find the optimal size of the traction motor, as it is done in [15], with the gear ratio as an additional design variable.

5.1. Methodology

To show the potential and usability of the proposed IM scaling scheme an IM in an electric vehicle is optimized. Changes of the machine configuration, such as the number of stator slots, are not considered to focus on the radial and axial scaling. The gear ratio, the axial length and the radius of the IM are used as the design parameters. The objective function that is minimized in the optimization process, considers the costs of the machine and the produced loss energy of the IM in the worldwide harmonized light vehicles test procedure (WLTP). Here, the costs of the machine and the loss energy are weighted with different factors. The Evolutionary Strategy is used as an optimization strategy. The procedure of it is shown in Fig. 11.

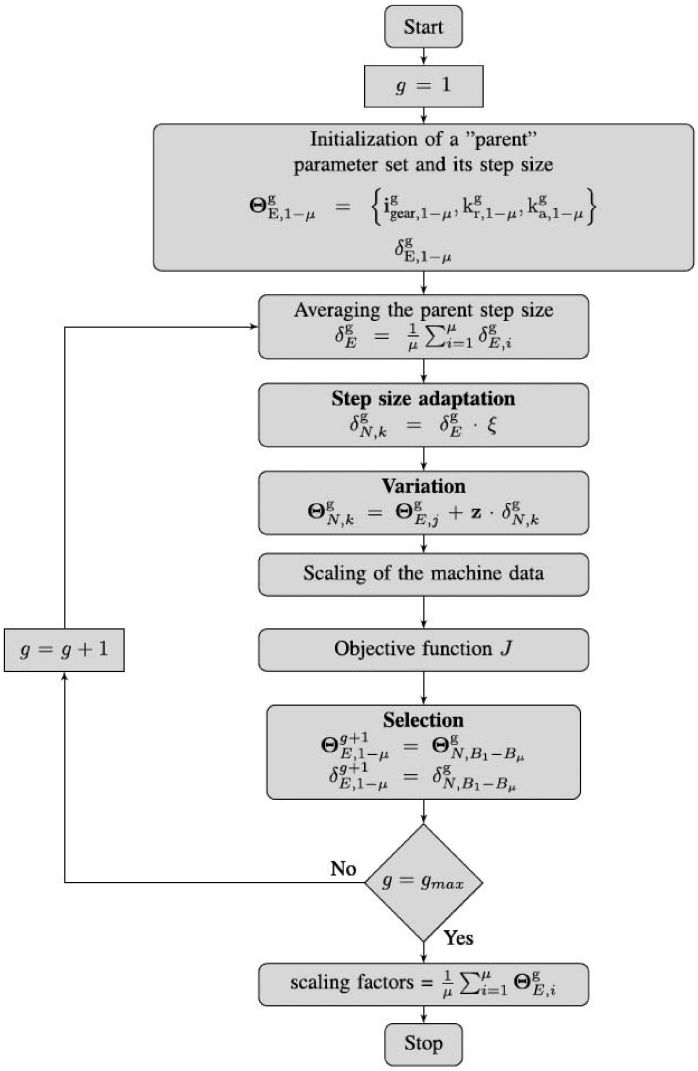

Fig. 11. Evolutionary strategy

It starts with the initialization of the parameter set $\mathbf{\Theta}^{g}_{E,1-\mu}$ and the step size of the parameters $\delta^{g}_{E,1-\mu}$, where μ is the number of the parents and g the generation number. For the initial parameters the radial and axial scaling factor are set to $k_r = k_a = 1$ and the gear ratio is set to $i_{\text{gear}} = 8$. The initial step size is set to a fourth of the initial parameter values. The step size is averaged in the second step and adapted by a logarithmic distributed random number. With the normal distributed random number z and the step size the new parameter sets $\mathbf{\Theta}^{g}_{N,k}$, named progenies, are calculated in the variation step. With the new parameters the machine is scaled, the gear ratio changed and the objective function is calculated. In the selection the best progenies become the new parents parameter and the calculation of the next generation is started. The process ends after a certain number of generations.

5.2. Results

The results of the design optimization with the Evolutionary Strategy is shown in Fig. 12. It shows the machines with different parameters of the radial scaling factor k_r, the axial scaling factor k_a and the gear ratio i_{gear} that results in the minimum objective function. All different parameter sets are marked with a gray point. The optimum parameter sets are marked by black dots. It can be seen that the optimization algorithm varies the three variable parameters in a wide range and converge fast towards an optimum region. The calculation of the objective function for every single parameter set, including the scaling of the IM's FE solutions, in Matlab takes a processor time of ca. 0.8 s, using an Intel(R) Core(TM) i7-6500U CPU @ 2.5 GHz and an 8 GB RAM.

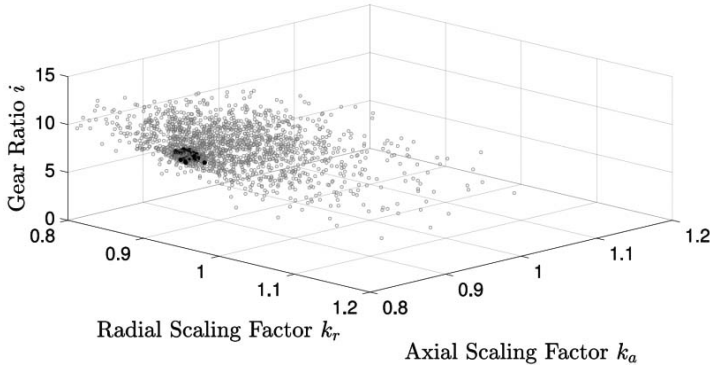

Fig. 12. Pareto front of the proposed optimization process

6. Conclusions

In this paper an IM scaling procedure for the machine's 2D FE solutions is proposed. Besides the geometrical scaling of the IM, the scaling laws for variations in the stator and rotor resistance, for the maximum speed and for the number of turns of the stator winding are presented. The reference FE solutions of the IM are scaled in the I_1-f_2-plane and transformed to the T-n-map, by considering boundary conditions, such as maximum current, and taking into account an operation

strategy. The results of the scaling process show a very good agreement with the FE results of the scaled IM. The scaling procedure is tested in the optimization of a traction drive. The results of the optimization show that the proposed scaling process is suitable for the use in numerical optimization processes.

The rotor resistance scaling can be used to analyze the machine's behavior for different rotor bar materials, their quality differences or different rotor temperatures. It can also be used in combination with a thermal model of the IM to calculate the IM's thermal behavior in difference operation conditions. The proposed scaling methodology is a rapid and very accurate tool to scale entire operation maps of IMs. In further work, the scaling laws for variations in the electrical steel due to temperature differences or the quality of the material will be studied. Furthermore, the limits of this method will be analyzed and the scaling will be validated for different machine configurations and designs, such as closed rotor slots. A validation with experimental results will be conducted. The focus of further publications can also be the optimization process itself.

References

[1] Mallik S., Mallik K., Barman A., Maiti D., Biswas S.K., Deb N.K., Basu S., *Efficiency and cost optimized design of an induction motor using genetic algorithm*, IEEE Transactions on Industrial Electronics, vol. 64, no. 12, pp. 9854–9863 (2017).

[2] Žarko D., *Design of premium efficiency (ie3) induction motors using evolutionary optimization and scaling laws*, Przeglad Elektrotechniczny, vol. 1, pp. 183–186 (2016).

[3] Einfuegen S., *Efficiency and cost optimized design of an induction motor using genetic algorithm*, IEEE Transactions on Industrial Electronics, vol. 64, no. 12, pp. 9854–9863 (2017).

[4] von Pfingsten G., Steentjes S., Hameyer K., *Operating point resolved loss calculation approach in saturated induction machines*, IEEE Transactions on Industrial Electronics, vol. 64, no. 3, pp. 2538–2546 (2017).

[5] Žarko D., Stipetič S., Martinovic M., Kovačić M., Jercic T., Hanic Z., *Reduction of computational efforts in finite element-based permanent magnet traction motor optimization*, IEEE Transactions on Industrial Electronics, vol. 65, no. 2, pp. 1799–1807 (2018).

[6] von Pfingsten G., Hameyer K., *Highly efficient approach to the simulation of variable-speed induction motor drives*, IET Science, Measurement Technology, vol. 11, no. 6, pp. 793–801 (2017).

[7] Wood R.W., *Scaling magnetic systems*, IEEE Transactions on Magnetics, vol. 47, no. 10, pp. 2685–2688 (2011).

[8] Hsieh K.T., Kim B.K., *One kind of scaling relations on electromechanical systems*, IEEE Transactions on Magnetics, vol. 33, no. 1, pp. 240–244 (1997).

[9] Stipetič S., Žarko D., Popescu M., *Ultra-fast axial and radial scaling of synchronous permanent magnet machines*, IET Electric Power Applications, vol. 10, no. 7, pp. 658–666 (2016).

[10] Alberti L., Bianchi N., Boglietti A., Cavagnino A., *Core axial lengthening as effective solution to improve the induction motor efficiency classes*, IEEE Transactions on Industry Applications, vol. 50, no. 1, pp. 218–225 (2014).

[11] Bone J.C.H., *Influence of rotor diameter and length on the rating of induction motors*, Electric Power Applications, IEE Journal on, vol. 1, no. 1, pp. 2–6 (1978).

[12] Lange E., Henrotte F., Hameyer K., *An efficient field-circuit coupling based on a temporary linearization of fe electrical machine models*, IEEE Transactions on Magnetics, vol. 45, no. 3, pp. 1258–1261 (2009).

[13] Williamson S., Begg M.C., *Calculation of the resistance of induction motor end rings*, IEE Proceedings B – Electric Power Applications, vol. 133, no. 2, pp. 54–60 (1986).

[14] Ramakrishnan K., Stipetič S., Gobbi M., Mastinu G., *Optimal sizing of traction motors using scalable electric machine model*, IEEE Transactions on Transportation Electrification, vol. 4, iss. 1, pp. 314–321 (2018).

[15] Ramakrishnan K., Stipetič S., Gobbi M., Mastinu G., *Multiobjective optimization of electric vehicle powertrain using scalable saturated motor model*, in 2016 Eleventh International Conference on Ecological Vehicles and Renewable Energies (EVER), Monte Carlo, Monaco, pp. 1–6 (2016).

[16] von Pfingsten G., Nell M., Hameyer K., *Hybrid simulation methods for induction machine calculation reduction of simulation effort by coupling static fea with transient fea and analytic formulations*, in 2017 18th International Symposium on Electromagnetic Fields in Mechatronics, Electrical and Electronic Engineering (ISEF) Book of Abstracts, Lodz, Poland, pp. 1–2 (2017).

[17] Stipetič S., Žarko D., Popescu M., *Scaling laws for synchronous permanent magnet machines*, in 2015 Tenth International Conference on Ecological Vehicles and Renewable Energies (EVER), Monte Carlo, Monaco, p. 1–7 (2015).

[18] Stipetič S., Goss J., *Calculation of efficiency maps using scalable saturated flux-linkage and loss model of a synchronous motor*, in 2016 XXII International Conference on Electrical Machines (ICEM), Lausanne, Switzerland, pp. 1380–1386 (2016).

[19] Žarko D., Kovačić M., Stipetič S., Vuljaj D., *Optimization of electric drives for traction applications*, in 2017 19th International Conference on Electrical Drives and Power Electronics (EDPE), Dubrovnik, Croatia, pp. 15–32 (2017).

[20] Nell M., Lenz J., Hameyer K., *Efficient numerical optimization of induction machines by scaled fe simulations*, in 2018 XIII International Conference on Electrical Machines (ICEM), Alexandroupoli, Greece, pp. 198–204 (2018).

[21] von Pfingsten G., Steentjes S., Hameyer K., *Transient approach to model operating point dependent losses in saturated induction machines*, in 2016 XXII International Conference on Electrical Machines (ICEM), Lausanne, Switzerland, pp. 626–632 (2016).

[22] Stipetič S., Miebach W., Žarko D., *Optimization in design of electric machines: Methodology and workflow*, in 2015 Intl Aegean Conference on Electrical Machines Power Electronics (ACEMP), 2015 Intl Conference on Optimization of Electrical Electronic Equipment (OPTIM) 2015 Intl Symposium on Advanced Electromechanical Motion Systems (ELECTROMOTION), Side, Turkey, pp. 441–448 (2015).